Supporting Information for:
Impacts and mechanisms of long-term water column changes on sediment–water nitrogen fluxes in semi-enclosed inland seas

Zhaosen Wu [1], Xinyu Guo [2, *], Masatoshi Nakakuni [3, 4], Kuninao Tada [3, 4]

[1]Key Laboratory of Marine Environment and Ecology, Ministry of Education of China, Ocean University of China, 238 Songling Road, Qingdao 266100, China

[2]Center for Marine Environmental Studies, Ehime University, 2-5 Bunkyo-Cho, Matsuyama 790-8577, Japan

[3]Faculty of Agriculture, Kagawa University, Ikenobe, Kita, Miki, Kagawa 761-0701, Japan

[4]Seto Inland Sea Regional Research Center, Kagawa University, Saiwai, Takamatsu, Kagawa 761-0016, Japan

* Corresponding Author: **Xinyu Guo** (Email: guo.xinyu.mz@ehime-u.ac.jp)

The supplementary material includes Text S1-S3; Figures S1−S13; Tables S1-S2.

Supplementary Texts

Text S1. Model framework and governing equations

A one-dimensional vertical sediment biogeochemical model was applied to simulate nitrogen cycling and sediment–water exchanges in Harima Nada. The model is based on early diagenetic theory and explicitly represents the coupled transport and transformation of particulate organic matter and dissolved nitrogen species within the sediment column (Berner, 1980).

The model domain consists of two parts: a solid one and a pore-water one (Figure S2). State variables include two types of particulate organic nitrogen (PON) with different degradability, dissolved oxygen (DO), ammonium (NH_4^+), nitrite (NO_2^-), nitrate (NO_3^-), and oxygen demand units (ODU). ODU is a lumped variable representing reduced metabolites (e.g., reduced Fe, Mn, and sulfur species) generated during anaerobic organic matter degradation, expressed in oxygen-equivalent units (Soetaert et al., 1996). In addition, a surface fluff layer is given to represent the biologically active layer where rapid recycling and exchanges with the overlying water occur (Kuhrts et al., 2006; Laima et al., 2002; Lee et al., 2002). The two types of PON are assumed to undergo first-order degradation at different rates, representing relatively labile and refractory organic matter, both of which are transported vertically through sedimentation, burial and bioturbation-induced mixing. Their mineralization provides the primary source of dissolved inorganic nitrogen within the sediment.

Dissolved species in pore water are transported through molecular diffusion, bioturbation, sedimentation and bioirrigation. The model resolves the major nitrogen transformation pathways occurring in coastal sediments, including organic matter mineralization, nitrification, denitrification, anaerobic ammonium oxidation (anammox), and dissimilatory nitrate reduction to ammonium (DNRA). In addition, the production, oxidation, and burial of reduced metabolites are represented through the ODU state variable (Soetaert et al., 1996).

The temporal evolution of particulate and dissolved substances is governed by advection–diffusion–reaction equations. The governing equations for solid ($C_s, \mathrm{mmol\ m^{-3}}$) and dissolved ($C_d, \mathrm{mmol\ m^{-3}}$) state variables are given in Equations (1) and (2), respectively. These equations include sedimentation, bioturbation, molecular diffusion, bioirrigation, and biogeochemical reaction terms. Because the study area is characterized by muddy sediments, pressure-driven pore-water advection is neglected.

$$\frac{\partial[(1-\emptyset)\cdot C_s]}{\partial t} = \frac{\partial[(1-\emptyset)\cdot D_B\cdot\frac{\partial C_s}{\partial z}]}{\partial z} - \frac{\partial[\omega\cdot(1-\emptyset)\cdot C_s]}{\partial z} + (1-\emptyset)\cdot\sum R_s \quad (1)$$

$$\frac{\partial[\emptyset\cdot C_d]}{\partial t} = \frac{\partial[\emptyset\cdot(D_B+D_M)\cdot\frac{\partial C_d}{\partial z}]}{\partial z} - \frac{\partial[\omega\cdot\emptyset\cdot C_d]}{\partial z} + \emptyset\cdot\alpha\cdot(C_d^w - C_d) + \emptyset\cdot\sum R_d \quad (2)$$

Where z (m) is vertical coordinate for sediment depth, t (s) is time, $\emptyset$ is the sediment porosity, D_B ($m^2\ s^{-1}$) is the bioturbation coefficient, D_M ($m^2\ s^{-1}$) is the molecular diffusion coefficient, ω ($m\ s^{-1}$) is the sedimentation velocity, α (s^{-1}) is the bioirrigation coefficient, C_d^w ($mmol\ m^{-3}$) is the concentration of dissolved matter in the bottom water, R_s is the biochemical reaction rate of PON, and R_d is the biochemical reaction rate of dissolved matter, including NH_4^+, NO_2^-, NO_3^-, DO and ODU.

Bioturbation intensity (D_B) decreases exponentially with sediment depth and is parameterized using Equation (3) (Radtke et al., 2019).

$$D_B(z) = \begin{cases} D_{B_{max}}, & 0 < z < z_{max} \\ D_{B_{max}}\cdot\exp\left(-\frac{z-z_{max}}{z_d}\right), & z \geq z_{max} \end{cases} \quad (3)$$

Where z_{max} (m) is the depth down to which the maximum bioturbation coefficient ($D_{B_{max}}$) is applied, z_d (m) is the decaying length scale of $D_{B_{max}}$ ($m^2\ s^{-1}$).

Molecular diffusion coefficients (D_M) are corrected for sediment tortuosity according to Equation (4), with temperature dependence described by Equation (5) (Boudreau et al., 1998; Radtke et al., 2019).

$$D_M(z) = \frac{D^T}{1-2.02\ln(\emptyset)} \quad (4)$$

$$D^T = D_0 + a\cdot T \quad (5)$$

where D^T and D_0 ($m^2\ s^{-1}$) is the diffusion coefficient of the dissolved matter in the particle-free liquid at T and 0 ℃, respectively. a ($m^2\ s^{-1}\ (℃)^{-1}$) is an ion-specific coefficient (Soetaert et al., 1996).

Bioirrigation is represented by a depth-dependent function (Equation (6)) (Dale et al., 2011).

$$\alpha(z) = \alpha_1\cdot\frac{\exp(\alpha_2-z)}{1+\exp(\alpha_2-z)} \quad (6)$$

The parameters α_1 (s^{-1}) and α_2 (m) represent the magnitude of bioirrigation and the depth at which it decreases to half of α_1, respectively.

Nitrogen transformation processes are described by Equations (7)–(12). Organic matter mineralization is partitioned among oxic mineralization, denitrification, anoxic mineralization. Following previous early

diagenetic modeling studies, limitation functions are normalized to ensure that the total degradation rate does not exceed the prescribed first-order mineralization rate (Soetaert et al., 1996). Temperature dependence is applied to organic matter mineralization, while the effects of temperature on other processes are represented indirectly through coupled biogeochemical interactions and temperature-dependent diffusion (Capet et al., 2016; Dale et al., 2011). Several pathway-partitioning and leakage coefficients are introduced to account for the incomplete conversion of nitrogen intermediates and the distribution of products among nitrate reduction pathways (Akbarzadeh et al., 2018). The complete reaction formulations are summarized in Table S1.

$$\sum R_{PON} = -R_{Min}^{OM} - R_{Den} - R_{Min}^{AM} - R_{DNRA} \quad (7)$$

$$\sum R_{NH_4^+} = R_{Min}^{OM} + R_{Den} + R_{Min}^{AM} - R_{Nit1} + (1 + 0.5 \cdot (1 - \delta) \cdot r_{C:N}) R_{DNRA} - R_{Ana} \quad (8)$$

$$\sum R_{NO_2^-} = 0.8 \cdot \alpha \cdot r_{C:N} \cdot R_{den} + R_{Nit1} - R_{Nit2} + 0.5 \cdot \delta \cdot r_{C:N} \cdot R_{DNRA} - R_{Ana} \quad (9)$$

$$\sum R_{NO_3^-} = R_{Nit2} - 0.8 \cdot r_{C:N} \cdot R_{den} - 0.5 \cdot r_{C:N} \cdot R_{DNRA} \quad (10)$$

$$\sum R_{O_2} = -r_{C:N} \cdot R_{Min}^{OM} - 1.5 \cdot R_{Nit1} - 0.5 \cdot R_{Nit2} - R_{ODUox} \quad (11)$$

$$\sum R_{ODU} = r_{C:N} \cdot (1 - r_{ODUsolid}) \cdot R_{Min}^{AM} - R_{ODUox} \quad (12)$$

Because benthic biomass and organic matter turnover are substantially enhanced within the fluff layer, mineralization rates in this layer are assumed to be higher than those in the underlying sediment (Kuhrts et al., 2006; Laima et al., 2002; Lee et al., 2002). The enhancement factor was set to 50 during model calibration and applied uniformly throughout the simulations.

At the sediment–water interface, particulate organic matter exchange is controlled by bottom shear stress. Organic particles settle into the fluff layer under low-stress conditions and are resuspended when bottom stress exceeds a critical threshold. The corresponding exchange flux (F_s) is calculated using Equation (13) (Wang, 2002).

$$F_s = \begin{cases} w \cdot C_s^w \cdot (\frac{\tau}{\tau_c} - 1), & \tau < \tau_c \\ E_s \cdot (\frac{\tau}{\tau_c} - 1), & \tau \geq \tau_c \end{cases} \quad (13)$$

where w ($m\ s^{-1}$) is the sinking velocity of particles in the bottom water, C_s^w ($mmol\ m^{-3}$) is concentration of PON in the bottom water, τ ($N\ m^{-2}$) is the bottom stress, τ_c ($N\ m^{-2}$) is the critical bottom stress, E_s ($mmol\ m^{-2}\ s^{-1}$) is the resuspension coefficient.

Dissolved substances are exchanged across the sediment–water interface through molecular diffusion, sediment mixing, and bioirrigation, with fluxes calculated from concentration gradients between pore water and bottom water (Equation (14)) (Boudreau et al., 1998).

$$F_d = -(D_{mix}^s + D_M^s) \cdot \emptyset \cdot \frac{C_d^w - C_d^{pw}}{\Delta z} \quad (14)$$

where D_{mix}^s ($m^2\ s^{-1}$) is the effective surface mixing coefficient accounting for sediment mixing processes such as bioturbation and resuspension, D_M^s ($m^2\ s^{-1}$) is the surface molecular coefficient, C_d^{pw} ($mmol\ m^{-3}$) is the concentration of dissolved matter in the pore water of fluff layer, Δz (m) is the distance of the diffusion layer at sediment-water interface.

At the lower boundary of the model domain, only the refractory PON fraction is allowed to leave the active sediment layer through burial (Equation (15)) (Radtke et al., 2019).

$$B_s = \omega \cdot (1 - \emptyset) \cdot C_s^b \quad (15)$$

where superscript of b represents the deepest layer of the model domain.

Diffusive exchanges of NH_4^+, NO_2^-, and ODU with deeper sediments are represented by Equation (16). Because deeper sediments are assumed to be permanently anoxic, diffusive fluxes of DO and NO_3^- across the lower boundary are set to zero.

$$B_d = -\left(D_B^b + D_M^b\right) \cdot \emptyset \cdot \frac{C_d^b - C_d^{bc}}{\Delta z^b} \quad (16)$$

where C_d^{bc} are the concentrations in the pore water under the deepest layer of the model domain ($mmol\ m^{-3}$), whose values are given from observations.

All model parameters and reaction coefficients are listed in Tables S2., and the sensitivity analysis is presented in Figure S3.

Text S2. Initial concentration of state variables and input profiles in the model

Given that particle organic nitrogen (PON) constitutes over 99% of the total nitrogen (TN) in sediments, the TN concentration profile was designated as the initial PON profile. The TN concentration observed in 1990 exhibited a maximum value at the sediment surface and remained nearly constant between depths

of 17 and 80 cm. This stable region was interpreted as representing slow-decayed PON and was used for exponential fitting. The difference between the observed TN and the slow-decayed PON was attributed to fast-decayed PON. The ammonium (NH_4^+) concentration profile in July 1992 was generated through linear interpolation of the observed data.

Due to the absence of earlier measurements, additional profiles of NO_x^- concentration and porosity were obtained from observations made in July 2019, while DO concentrations in 2000. Considering the rapid depletion of NO_3^- concentration to zero under anaerobic conditions, and based on the DO profile, the NO_x^- (NO_2^-+NO_3^-) concentrations within the upper 2 cm sediment layer was employed for linear fitting to establish the NO_3^- concentration profile. The NO_2^- concentration profile was subsequently derived by subtracting the NO_3^- concentration profile from the observed NO_x^-. Furthermore, the model incorporated DO concentration and porosity profile data as inputs for calculations, as illustrated in Figure S4, where DO concentration was confined to the upper 2 mm sediment layer.

Text S3. Estimation of interannual variations in sediment mineralization rate

Interannual variation in sedimentary PON concentration is primarily governed by the PON flux at the sediment-water interface and the amount of mineralization within the sediment. The former is largely influenced by the PON concentration in bottom water, while the latter depends on the coefficient of mineralization rate (Rm, s^{-1}). Therefore, by conducting numerical experiments with different combinations of bottom water PON concentrations and sediment mineralization rates, we can determine the corresponding steady-state sedimentary PON concentrations.

Based on the observed range of bottom water PON concentrations in the Seto Inland Sea over the past 40 years, we set the values of 1, 3, 5, 7, and 9 mmol m^{-3}. After many times of trial and error, we obtained a representative pair of mineralization rates corresponding to fast-decaying and slow-decaying PON under steady-state conditions in Harima Nada in 2020 (PON_f as 2.8×10^{-9} s^{-1} and PON_s as 1×10^{-9} s^{-1}). These standard rates were scaled by factors of 0.5, 1, 2, 3, 4, 6, 8, and 10 for sensitivity experiments.

The results showed that each unique combination of bottom water PON concentration and sediment mineralization rate produced a distinct sediment PON concentration. Specifically, when the mineralization rate is held constant, higher bottom water PON concentrations lead to increased PON

fluxes and higher sedimentary PON concentrations, with the results align along straight lines (Figure S5a). Conversely, when the bottom water PON concentration is fixed, the PON flux remains unchanged, and higher mineralization rates result in lower sediment PON concentrations.

Since the 1980s, the Japanese Ministry of the Environment has conducted high-resolution sediment surveys in the Seto Inland Sea every decade. By comparing observed PON concentrations in bottom water and sediments at station NH with results from our sensitivity experiments, we estimated the interannual variation in sediment mineralization rates (Figure S5b). The analysis revealed a strong linear relationship between the sediment mineralization rate and the ratio of bottom water PON concentration to sediment PON concentration (Figure S5c). Under steady-state assumptions, the derived analytical relationship is:

$$\mathrm{Rm} = \frac{w_{sink}}{H} \cdot \frac{PON^{bw}}{PON^{sed}} - \frac{w_{burial}}{H} \quad (17)$$

Where w_{sink} is the particle sinking velocity in the water column ($m\,s^{-1}$), PON^{bw} and PON^{sed} ($mmol\,m^{-3}$) are PON concentration in bottom water and sediment respectively, H (m) is the thickness of the sediment model domain, w_{burial} ($m\,s^{-1}$) is the burial velocity.

According to this analysis, the sediment mineralization rate in Harima Nada experienced a sharp decline from the 1980s to the 1990s, followed by a gradual decrease until 2001, and then a steady increase until 2015 (Figure S5d).

Supplementary Figures

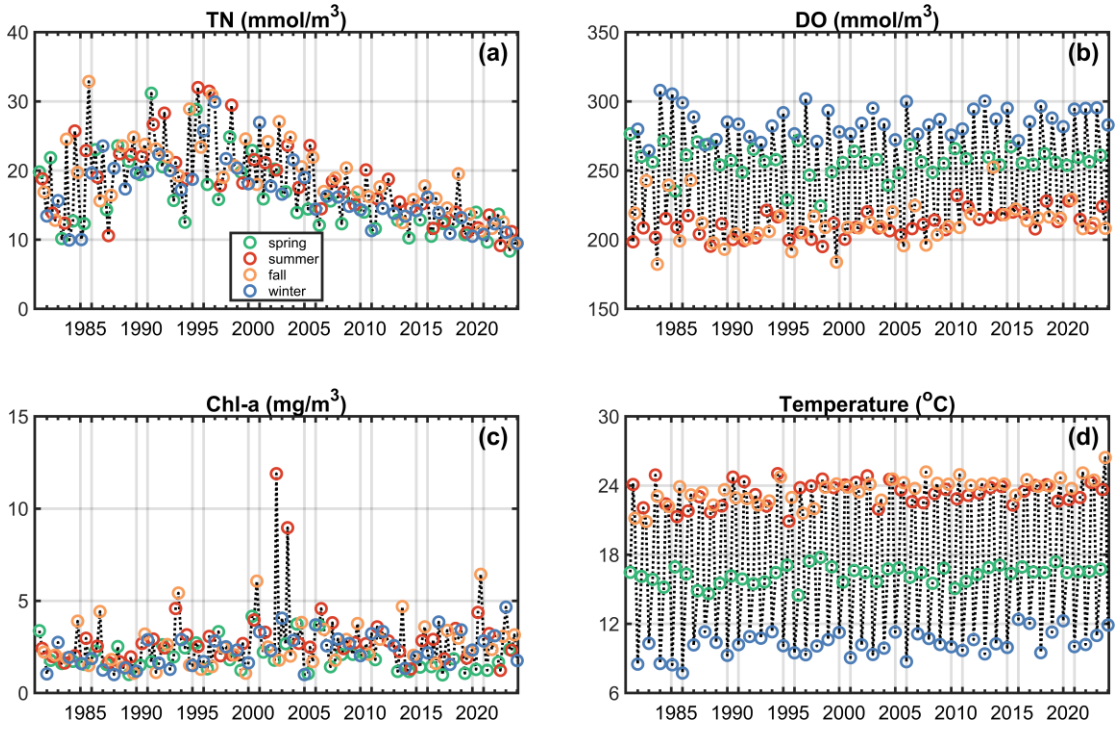


Figure S1. Interannual variations of (a) total nitrogen, (b) dissolved oxygen, (c) chlorophyll-a, and (d) temperature in the water column of Harima Nada from 1981 to 2023.

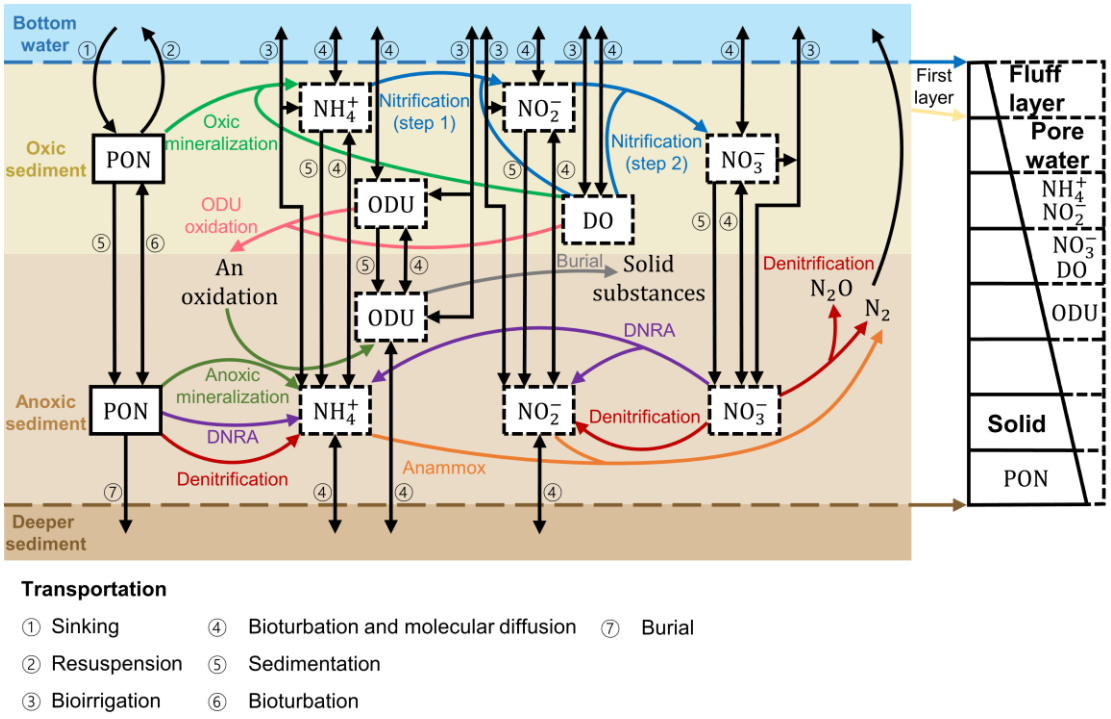
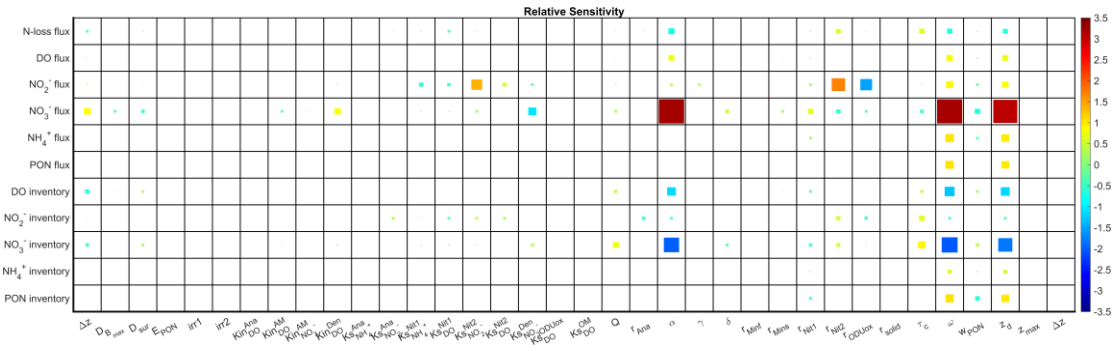


Figure S2. Physical and biogeochemical processes for nitrogen cycle in the sediment model. Six state variables in the model are PON, NH_4^+, NO_2^-, NO_3^-, DO and ODU (the oxygen demand units). PON is a solid substance (enclosed by solid lines), while NH_4^+, NO_2^-, NO_3^-, DO and ODU are dissolved substances in the pore water (enclosed by dash lines). The physical processes and biogeochemical processes are denoted by black arrows and colored arrows, respectively. The numbers with circle denote the transport processes included in the model. The panel on the right represents the sediment separated into two distinct phases: solid and dissolved components, with porosity diminishing with increasing depth. The surface layer of the model is identified as the fluff layer.



182

183 **Figure S3.** Sensitivity Analysis. The percentage change in the annual average of the main results when the parameter

184 changes by 1%. The expression for relative sensitivity (E_{ij}) is $E_{ij} = \frac{\Delta Y_j / Y_j}{\Delta X_i / X_i}$, where Y_j represents the model results

185 given along the y-axis, X_i represents the parameters along the x-axis, and E_{ij} is represented by the colour and size

186 of the block in the grid point corresponding to X_i and Y_j. No colour indicates that E_{ij} is less than 1%.

187

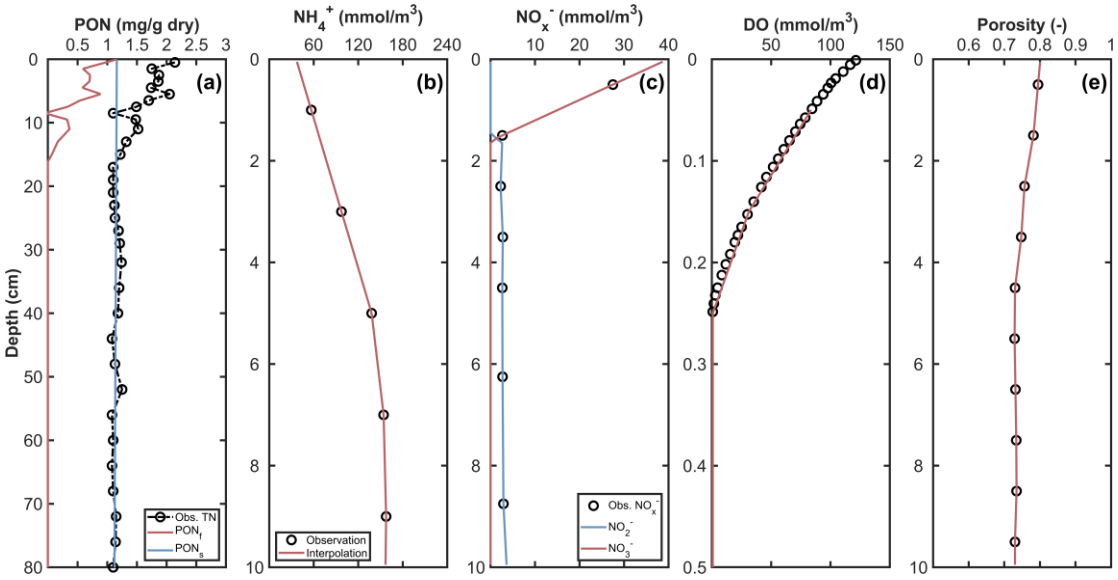


Figure S4. Initial and input profiles for the sediment model: (a) PON; (b) NH_4^+; (c) NO_3^- and NO_2^-; (d) DO; (e) porosity.

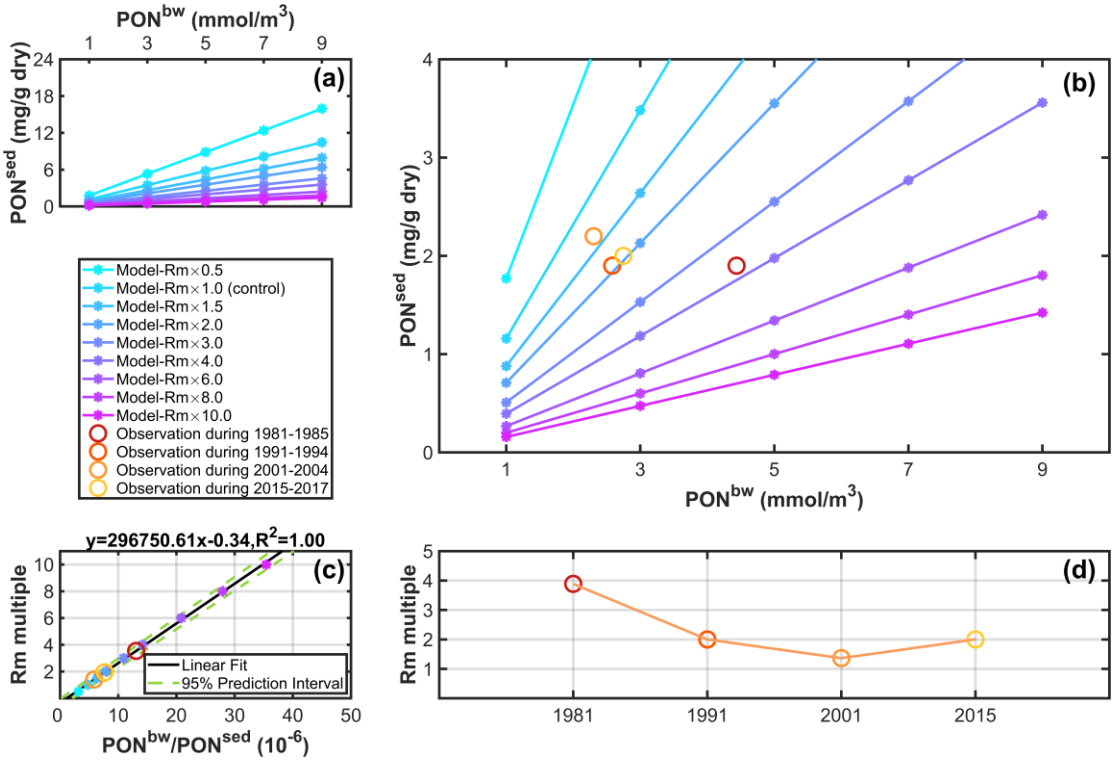


Figure S5. (a) Average concentration of sediment PON (PON^{sed}) at steady state under different bottom water PON concentrations (PON^{bw}) and sediment mineralization rate (Rm). In the control group, the combination for Rm is PON_f as 2.8×10^{-9} s^{-1} and PON_s as 1×10^{-9} s^{-1}. (b) PON^{sed} ranges from 0 to 4 mg/g dry weight, which corresponds to its observed range near station NH in Harima Nada across four decades with the observed data from the Japanese Ministry of the Environment (https://www.env.go.jp/water/heisa/heisa_net/setouchiNet/seto/g2/g2cat01/teishitsuodaku/index.html). (c) Linear regression analysis of Rm multiple versus the ratio of PON^{bw} to PON^{sed} with the observations. (d) Estimated Rm multiple from 1981 to 2015.

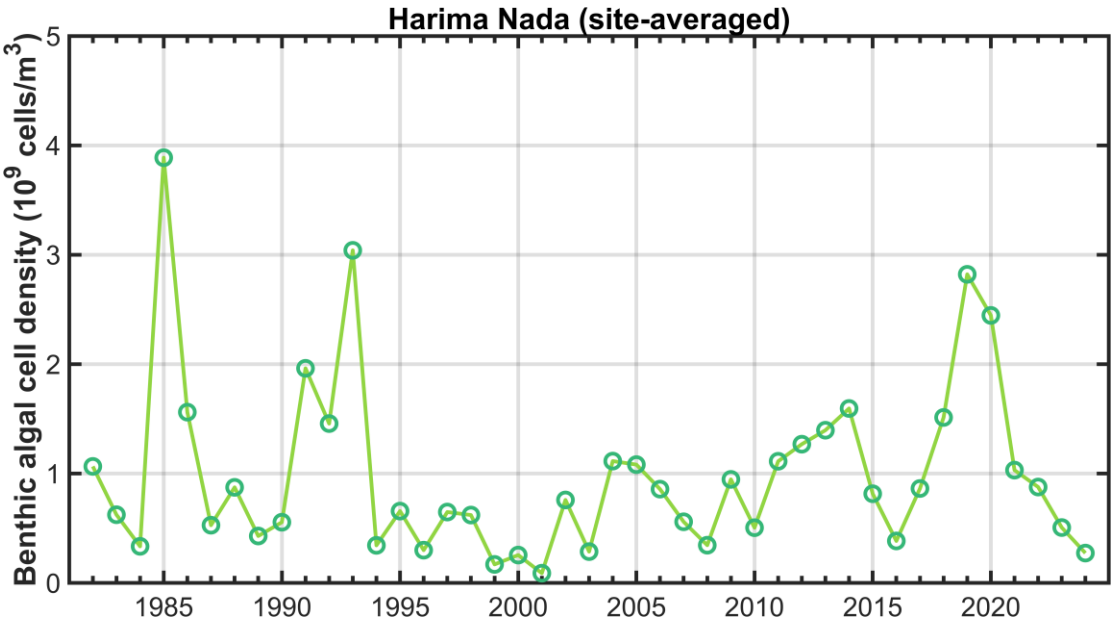


Figure S6. Interannual variation in the site-average cell density of benthic algal in Harima Nada from 1982 to 2024 based on more than four decades of seasonal monitoring data provided by the Japanese Ministry of the Environment (https://water-pub.env.go.jp/water-pub/mizu-site/mizu/kouiki/dataMap.asp).

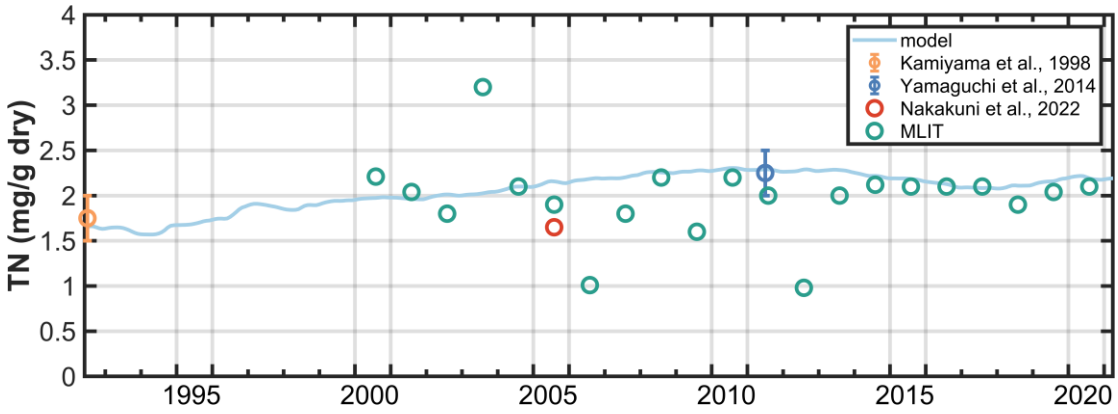


Figure S7. Interannual variation in the annual mean concentration of total nitrogen in Harima Nada from July 1992 to January 2021. The observational data are obtained from three research papers (Kamiyama et al., 1998; Nakakuni et al., 2022; Yamaguchi et al., 2014) and the dataset of the Ministry of Land, Infrastructure, Transport and Tourism (MLIT, https://www.pa.cgr.mlit.go.jp/suishitu/download/download_te.html).

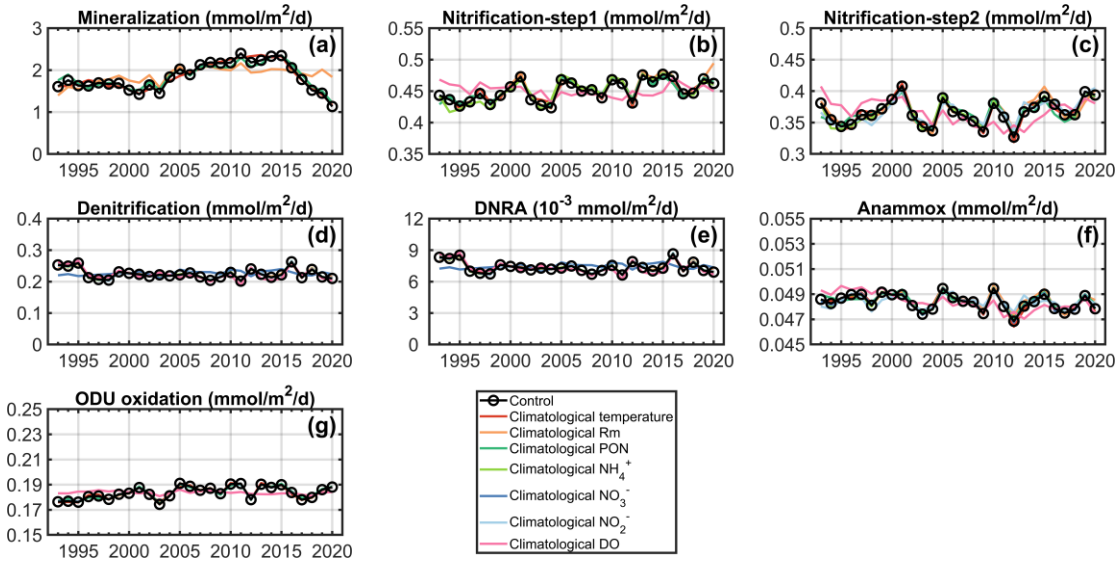


Figure S8. Comparisons of the biogeochemical rates among eight calculations (seven sensitivity experiments and one control run). The sensitivity experiments include the cases removing the interannual variations of water temperature (red, "Climatological temperature"), PON concentration (dark green, "Climatological PON"), NH_4^+ concentration (light green, "Climatological NH_4^+"), NO_3^- concentration (dark blue, "Climatological NO_3^-"), NO_2^- concentration (light blue, "Climatological NO_2^-"), and DO concentration (pink, "Climatological") in the overlying water, as well as of the mineralization rate (orange, "Climatological Rm"). (a) oxic and anoxic mineralization; (b) nitrification-step1; (c) nitrification-step2; (d) denitrification; (e) DNRA; (f) anammox; (g) ODU oxidation.

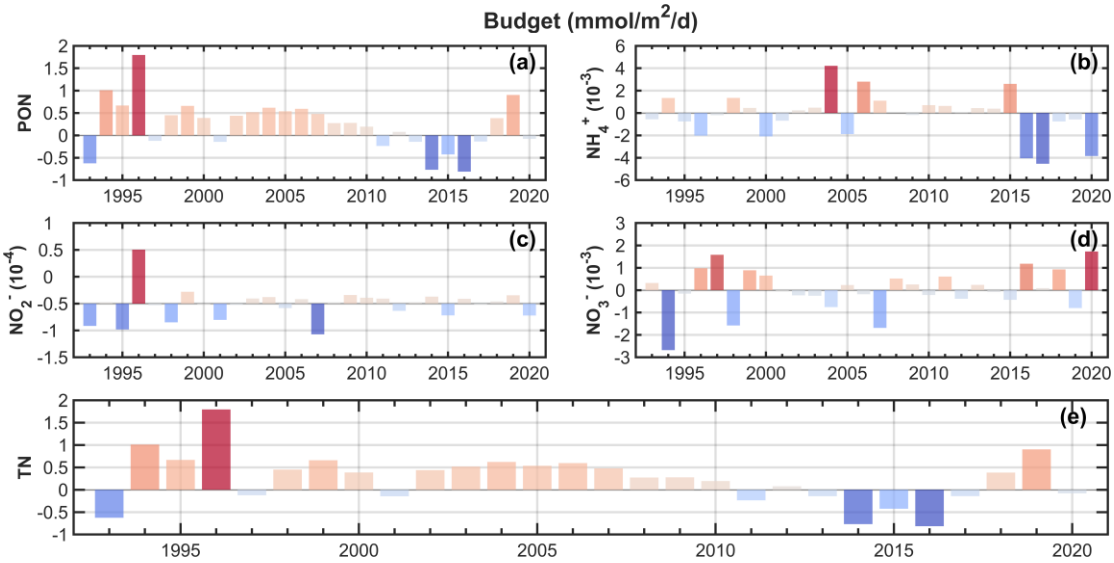


Figure S9. Interannual variation of sediment nitrogen budgets: (a) PON; (b) NH_4^+; (c) NO_2^-; (d) NO_3^-; (e) total nitrogen (TN).

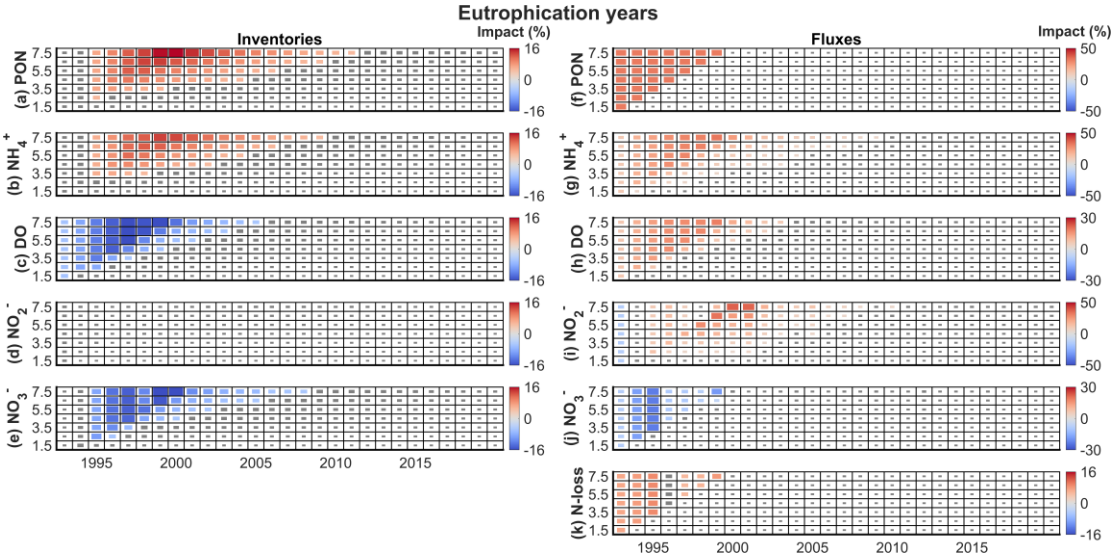


Figure S10. Sensitivity of sediment nitrogen inventories and sediment–water nitrogen fluxes to eutrophication duration. In the experiments, bottom-water total nitrogen concentration (TN^{bw}) was fixed at 130% of the non-eutrophic level, while the eutrophication duration varied from 1.5 to 7.5 years. The impact represents the relative difference between the eutrophic and non-eutrophic simulations on (a) PON inventory; (b) NH_4^+ inventory; (c) DO inventory; (d) NO_2^- inventory; (e) NO_3^- inventory; (f) PON flux; (g) NH_4^+ flux; (h) DO flux; (i) NO_2^- flux; (j) NO_3^- flux; (k) N-loss flux.

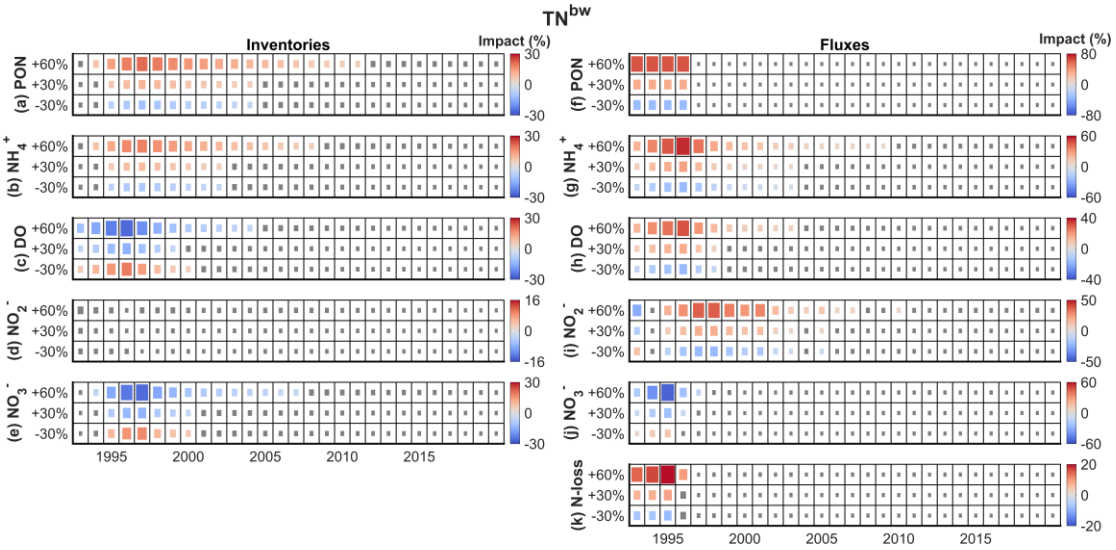


Figure S11. Sensitivity of sediment nitrogen inventories and sediment–water nitrogen fluxes to eutrophication severity. In the experiments, the eutrophication duration was fixed at 4.5 years, while TN^{bw} varied from 70% to 160% of the non-eutrophic level. The impact represents the relative difference between the eutrophic and non-eutrophic simulations on (a) PON inventory; (b) NH_4^+ inventory; (c) DO inventory; (d) NO_2^- inventory; (e) NO_3^- inventory; (f) PON flux; (g) NH_4^+ flux; (h) DO flux; (i) NO_2^- flux; (j) NO_3^- flux; (k) N-loss flux.

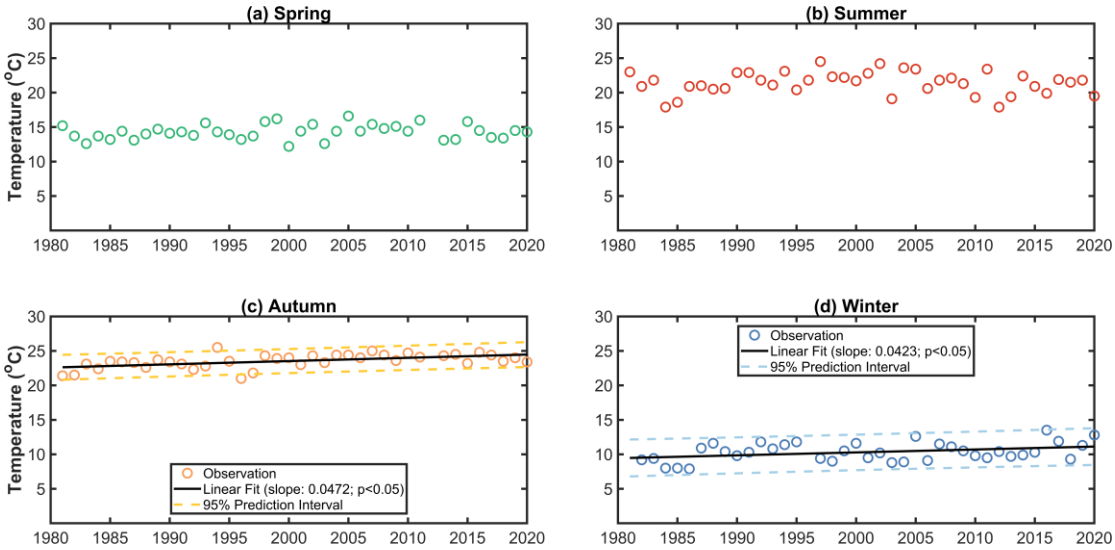


Figure S12. Observed bottom-water temperature in Harima Nada in (a) spring, (b) summer, (c) autumn and (d) winter from 1981 to 2020. The water temperature during the autumn and winter seasons exhibits a pronounced increasing trend.

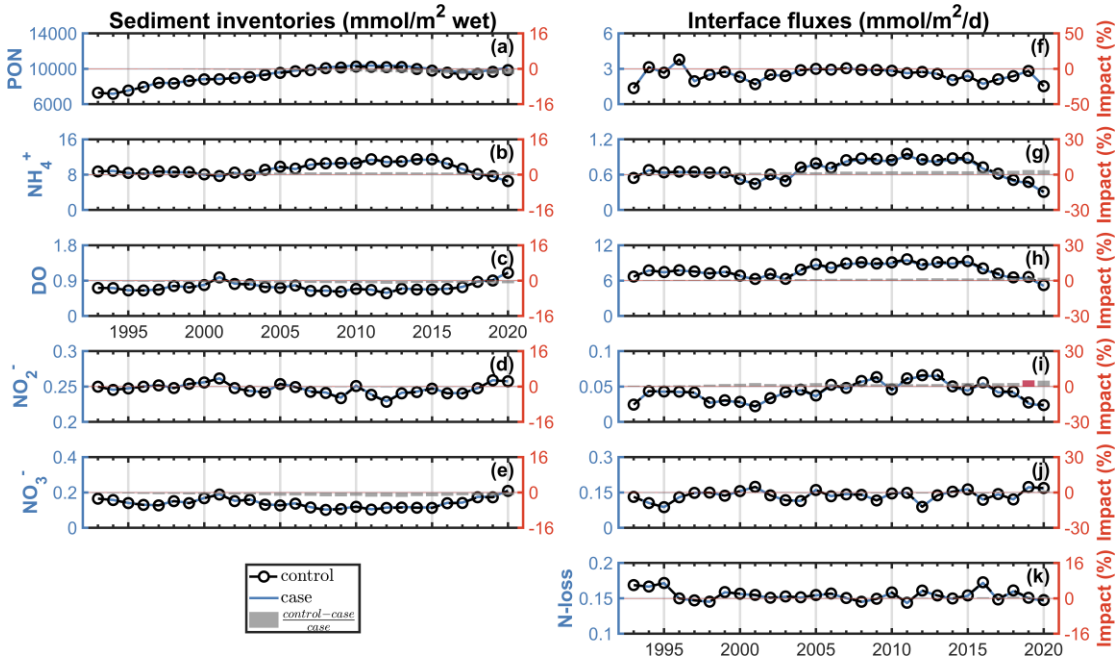


Figure S13. Comparisons of the model results between control run (water warming scenario) and non-water warming scenario: (a) PON inventory; (b) NH_4^+ inventory; (c) DO inventory; (d) NO_2^- inventory; (e) NO_3^- inventory; (f) PON flux; (g) NH_4^+ flux; (h) DO flux; (i) NO_2^- flux; (j) NO_3^- flux; (k) N-loss flux. The red bars indicate relative change exceeding 5% and the gray bars denote values with an absolute magnitude less than 5%.

Supplementary Tables

Table S1. Reaction formulas and rate expressions.

Process	Formula	Rate expression
Oxic mineralization (R_{Min}^{OM})	$(CH_2O)_x(NH_3)_y + xO_2 \rightarrow yNH_4^+ + (x-y)CO_2 + yHCO_3^- + (x-y)H_2O$	$R_{Min}^{OM} = r_{min} \cdot PON \cdot Q^{\frac{T-20}{10}} \cdot \frac{O_2}{O_2 + Ks_{O_2}^{OM}} \cdot \frac{1}{\sum lim}$
Denitrification (R_{Den})	$(CH_2O)_x(NH_3)_y + 0.8xNO_3^- \rightarrow yNH_4^+ + 0.8\alpha xNO_2^- + 0.4(1-\alpha-\beta)xN_2 + 0.4\beta xN_2O + (0.2x - y + 0.8\alpha x)CO_2 + (0.8x - 0.8\alpha x + y)HCO_3^- + (0.6x - y - 0.8\alpha x - 0.4\beta x)H_2O + (0.8\alpha x - 0.4\beta x)H_2$	$R_{Den} = r_{min} \cdot PON \cdot Q^{\frac{T-20}{10}} \cdot \frac{NO_3^-}{NO_3^- + Ks_{NO_3^-}^{Den}} \cdot \frac{Kin_{O_2}^{Den}}{O_2 + Kin_{O_2}^{Den}} \cdot \frac{1}{\sum lim} \cdot \gamma$
Anoxic mineralization (R_{Min}^{AM})	$(CH_2O)_x(NH_3)_y + \text{an oxidant} \rightarrow yNH_4^+ + xCO_2 + xODU + xH_2O$	$R_{Min}^{AM} = r_{min} \cdot PON \cdot Q^{\frac{T-20}{10}} \cdot \frac{Kin_{O_2}^{AM}}{O_2 + Kin_{O_2}^{AM}} \cdot \frac{Kin_{NO_3^-}^{AM}}{NO_3^- + Kin_{NO_3^-}^{AM}} \cdot \frac{1}{\sum lim}$
Nitrification_step1 (R_{Nit1})	$NH_4^+ + 1.5O_2 + 2HCO_3^- \rightarrow NO_2^- + 3H_2O + 2CO_2$	$R_{Nit1} = r_{nit1} \cdot \frac{NH_4^+}{NH_4^+ + Ks_{NH_4^+}^{Nit1}} \cdot \frac{O_2}{O_2 + Ks_{O_2}^{Nit1}}$

Nitrification_step2 (R_{Nit2})	$NO_2^- + 0.5O_2 \rightarrow NO_3^-$	$R_{Nit2} = r_{nit2} \cdot \frac{NO_2^-}{NO_2^- + Ks_{NO_2^-}^{Nit2}} \cdot \frac{O_2}{O_2 + Ks_{O_2}^{Nit2}}$
DNRA (R_{DNRA})	$(CH_2O)_x(NH_3)_y + 0.5xNO_3^- + (1-\delta)xH^+ \rightarrow (0.5(1-\delta)x + y)NH_4^+ + 0.5\delta xNO_2^- + yHCO_3^- + (x-y)CO_2 + (0.5x - y - \delta x)H_2O + 1.5\delta xH_2$	$R_{DNRA} = r_{min} \cdot PON \cdot Q^{\frac{T-20}{10}} \cdot \frac{NO_3^-}{NO_3^- + Ks_{NO_3^-}^{Den}} \cdot \frac{Kin_{O_2}^{Den}}{O_2 + Kin_{O_2}^{Den}} \cdot \frac{1}{\sum lim} \cdot (1-\gamma)$
Anammox (R_{Ana})	$NH_4^+ + NO_2^- \rightarrow N_2 + 2H_2O$	$R_{Ana} = r_{Ana} \cdot \frac{NH_4^+}{NH_4^+ + Ks_{NH_4^+}^{Ana}} \cdot \frac{NO_2^-}{NO_2^- + Ks_{NO_2^-}^{Ana}} \cdot \frac{Kin_{O_2}^{Ana}}{O_2 + Kin_{O_2}^{Ana}}$
ODU oxidation (R_{ODUox})	$ODU + O_2 \rightarrow$ an oxidant	$R_{ODUox} = r_{ODUox} \cdot ODU \cdot \frac{O_2}{O_2 + Ks_{O_2}^{ODUox}}$

263 $\sum lim = \frac{O_2}{O_2+Ks_{O_2}^{OM}} + \frac{NO_3^-}{NO_3^-+Ks_{NO_3^-}^{Den}} \cdot \frac{Kin_{O_2}^{Den}}{O_2+Kin_{O_2}^{Den}} + \frac{Kin_{O_2}^{AM}}{O_2+Kin_{O_2}^{AM}} \cdot \frac{Kin_{NO_3^-}^{AM}}{NO_3^-+Kin_{NO_3^-}^{AM}}$. $\sum lim$ is used to rescale competing

264 mineralization pathway, ensuring that the combined mineralization rate does not exceed the maximum

265 first-order degradation rate (Soetaert et al., 1996).

266 x:y denotes the molar C:N ratio of organic matter.

267

268

Table S2. Model parameters. (L: based on literature; M: constrained with the model, I: independently determined from observations).

Parameter	Value	Unit	Description	References
ω	8.24×10^{-11}	m s^{-1}	Sedimentation velocity	L[a]
$D_{B_{max}}$	2×10^{-11}	m^2 s^{-1}	Maximum bioturbation coefficient	M
z_{max}	0.05	m	Depth down to which the maximum bioturbation coefficient is applied	L[b]
z_d	0.05	m	Decaying length scale of the maximum bioturbation coefficient	L[b, d]
$D_0^{NH_4^+}$	9.80×10^{-10}	m^2 s^{-1}	The molecular diffusion coefficient of NH_4^+ in a particle-free solution at 0 ℃	L[b]
$D_0^{NO_2^-}$	9.16×10^{-10}	m^2 s^{-1}	The molecular diffusion coefficient of NO_2^- in a particle-free solution at 0 ℃	L[c]
$D_0^{NO_3^-}$	9.78×10^{-10}	m^2 s^{-1}	The molecular diffusion coefficient of NO_3^- in a particle-free solution at 0 ℃	L[b]
D_0^{DO}	1.11×10^{-9}	m^2 s^{-1}	The molecular diffusion coefficient of DO (dissolved oxygen) in a particle-free solution at 0 ℃	L[b]
D_0^{ODU}	9.74×10^{-10}	m^2 s^{-1}	The molecular diffusion coefficient of ODU (the oxygen demand units) in a particle-free solution at 0 ℃	L[b]

$a_{NH_4^+}$	3.89×10^{-11}	$m^2\ s^{-1}\ (°C)^{-1}$	Coefficient for temperature dependency of diffusion coefficient of NH_4^+	L[b]
$a_{NO_2^-}$	3.89×10^{-11}	$m^2\ s^{-1}\ (°C)^{-1}$	Coefficient for temperature dependency of diffusion coefficient of NO_2^-	L[b]
$a_{NO_3^-}$	3.89×10^{-11}	$m^2\ s^{-1}\ (°C)^{-1}$	Coefficient for temperature dependency of diffusion coefficient of NO_3^-	L[b]
a_{DO}	4.47×10^{-11}	$m^2\ s^{-1}\ (°C)^{-1}$	Coefficient for temperature dependency of diffusion coefficient of DO	L[b]
a_{ODU}	2.80×10^{-11}	$m^2\ s^{-1}\ (°C)^{-1}$	Coefficient for temperature dependency of diffusion coefficient of ODU	L[b]
α_1	1.16×10^{-7}	s^{-1}	The magnitude of bioirrigation	M
α_2	0.09	m	the depth at which bioirrigation coefficient decreases to half of α_1	L[d]
r_{minf}	3×10^{-8}	s^{-1}	Mineralization coefficient of fast decay organic nitrogen	M
r_{mins}	7×10^{-10}	s^{-1}	Mineralization coefficient of slow decay organic nitrogen	M
Q	2		Factor for temperature effect on mineralization	L[e]
$Ks_{O_2}^{OM}$	3	$mmol\ m^{-3}$	Half saturation constant of DO in oxic mineralization	L[b]

$Ks_{NO_3^-}^{Den}$	30	mmol m^{-3}	Half saturation constant of NO_3^- in denitrification	L[b]
$Kin_{O_2}^{Den}$	10	mmol m^{-3}	Half saturation constant of DO in denitrification	L[b]
α	5	%	Nitrite leakage during denitrification	L[c]
β	1	%	Nitrous oxide leakage during denitrification	L[c]
γ	95	%	Fraction of total NO_3^- Reduction occurring via denitrification	L[c]
$Kin_{O_2}^{AM}$	5	mmol m^{-3}	Half saturation constant of DO in anoxic mineralization	L[b]
$Kin_{NO_3^-}^{AM_}$	5	mmol m^{-3}	Half saturation constant of NO_3^- in anoxic mineralization	L[b]
r_{nit1}	1.16×10^{-4}	mmol m^{-3} s^{-1}	Maximum coefficient of nitrification (step 1)	M
r_{nit2}	1.16×10^{-3}	mmol m^{-3} s^{-1}	Maximum coefficient of nitrification (step 2)	M
$Ks_{NH_4^+}^{Nit1}$	10	mmol m^{-3}	Half saturation constant of NH_4^+ in nitrification (step 1)	L[c]
$Ks_{O_2}^{Nit1}$	15.6	mmol m^{-3}	Half saturation constant of DO in nitrification (step 1)	L[c]

$Ks_{NO_2^-}^{Nit2}$	10	mmol m^{-3}	Half saturation constant of NO_2^- in nitrification (step 2)	L[c]
$Ks_{O_2}^{Nit2}$	34.4	mmol m^{-3}	Half saturation constant of DO in nitrification (step 2)	L[c]
δ	5	%	Nitrite leakage during DNRA	L[c]
r_{Ana}	2.31×10^{-5}	mmol m^{-3} s^{-1}	Maximum anammox coefficient	M
$Ks_{NH_4^+}^{Ana}$	5	mmol m^{-3}	Half saturation constant of NH_4^+ in anammox	L[c]
$Ks_{NO_2^-}^{Ana}$	5	mmol m^{-3}	Half saturation constant of NO_2^- in anammox	L[c]
$Kin_{O_2}^{Ana}$	8	mmol m^{-3}	Half saturation constant of DO in anammox	L[c]
r_{ODUox}	1.16×10^{-5}	s^{-1}	Maximum ODU oxidation coefficient	L[f]
$Ks_{O_2}^{ODUox}$	1	mmol m^{-3}	Half saturation constant of DO in ODU oxidation	L[b]
$r_{ODUsolid}$	0.99	s^{-1}	Part of ODU production that is deposited as a solid	L[g]
$r_{C:N}$	10.2		Ratio of carbon to nitrogen	I
w	2.31×10^{-5}	m s^{-1}	Sinking velocity	L[h]
τ_c	0.06	N m^{-2}	Critical bottom stress	M
E_{PON}	1×10^{-8}	mmol m^{-2} s^{-1}	Resuspension coefficient	L[h]

D_{sur}	1×10^{-9}	$m^2\ s^{-1}$	Surface diffusion coefficient	M
Δz	3×10^{-3}	m	Distance of the diffusion layer at sediment-water interface	L[i]

[a] Ichimi et al. (2005) (Ichimi et al., 2005)

[b] Soetaert et al. (1996)

[c] Akbarzadeh et al. (2018)

[d] Dale et al. (2011)

[e] Capet et al. (2016)

[f] Laurent et al. (2016) (Laurent et al., 2016; Pastor et al., 2011)

[g] Pastor et al. (2011)

[h] Ding et al. (2020) (Ding et al., 2020)

[i] Wang et al. (2016) (Wang et al., 2016)

Reference

Akbarzadeh, Z., Laverman, A.M., Rezanezhad, F., Raimonet, M., Viollier, E., Shafei, B., Van Cappellen, P., 2018. Benthic nitrite exchanges in the Seine River (France): An early diagenetic modeling analysis. Sci Total Environ 628-629, 580-593. doi.org/10.1016/j.scitotenv.2018.01.319.

Berner, R., 1980. Early diagenesis: a theoretical approach: Princeton.

Boudreau, B.P., Mucci, A., Sundby, B., Luther, G.W., Silverberg, N., 1998. Comparative diagenesis at three sites on the Canadian continental margin. J. Mar. Res. 56(6), 1259-1284. doi.org/10.1357/002224098765093634.

Capet, A., Meysman, F.J.R., Akoumianaki, I., Soetaert, K., Grégoire, M., 2016. Integrating sediment biogeochemistry into 3D oceanic models: A study of benthic-pelagic coupling in the Black Sea. Ocean Modelling 101, 83-100. doi.org/10.1016/j.ocemod.2016.03.006.

Dale, A.W., Sommer, S., Bohlen, L., Treude, T., Bertics, V.J., Bange, H.W., Pfannkuche, O., Schorp, T., Mattsdotter, M., Wallmann, K., 2011. Rates and regulation of nitrogen cycling in seasonally hypoxic sediments during winter (Boknis Eck, SW Baltic Sea): Sensitivity to environmental variables. Estuar. Coast. Shelf Sci. 95(1), 14-28. doi.org/10.1016/j.ecss.2011.05.016.

Ding, X., Guo, X., Zhang, C., Yao, X., Liu, S., Shi, J., Luo, C., Yu, X., Yu, Y., Gao, H., 2020. Water conservancy project on the Yellow River modifies the seasonal variation of Chlorophyll-a in the Bohai Sea. Chemosphere 254, 126846. doi.org/10.1016/j.chemosphere.2020.126846.

Ichimi, K., Tada, K., Montani, S., 2005. The phytoplankton assemblage of the past and present in the Seto Inland Sea-the expectation from sediment core samples. Aquabiology 27(3), 214～221.

Kamiyama, T., Tsujino, M., Tamai, K., 1998. Estimation of bottom fluxes of several nutrients in Harima Nada, the Seto Inland Sea of Japan. Bulletin of the Nansei National Fisheries Research Institute (Japan)(31).

Kuhrts, C., Seifert, T., Fennel, W., 2006. Modeling Transport of Fluff Layer Material in the Baltic Sea. Hydrobiologia 554(1), 25-30. doi.org/10.1007/s10750-005-1003-x.

Laima, M., Maksymowska-Brossard, D., Sauriau, P.-G., Richard, P., Girard, M., Gouleau, D., Joassard, L., 2002. Fluff deposition on intertidal sediments: effects on benthic biota, ammonium fluxes and nitrification rates. Biogeochemistry 61(2), 115-133. doi.org/10.1023/a:1020264414924.

309 Laurent, A., Fennel, K., Wilson, R., Lehrter, J., Devereux, R., 2016. Parameterization of biogeochemical
310 sediment–water fluxes using in situ measurements and a diagenetic model. Biogeosciences 13(1), 77-94.
311 doi.org/10.5194/bg-13-77-2016.
312 Lee, J.-Y., Tett, P., Jones, K., Jones, S., Luyten, P., Smith, C., Wild-Allen, K., 2002. The PROWQM
313 physical–biological model with benthic–pelagic coupling applied to the northern North Sea. J. Sea Res.
314 48(4), 287-331. doi.org/https://doi.org/10.1016/S1385-1101(02)00182-X.
315 Nakakuni, M., Loassachan, N., Ichimi, K., Nagao, S., Tada, K., 2022. Biophilic elements in core
316 sediments as records of coastal eutrophication in the Seto Inland Sea, Japan. Regional Studies in Marine
317 Science 50. doi.org/10.1016/j.rsma.2021.102093.
318 Pastor, L., Cathalot, C., Deflandre, B., Viollier, E., Soetaert, K., Meysman, F.J.R., Ulses, C., Metzger,
319 E., Rabouille, C., 2011. Modeling biogeochemical processes in sediments from the Rhône River prodelta
320 area (NW Mediterranean Sea). Biogeosciences 8(5), 1351-1366. doi.org/10.5194/bg-8-1351-2011.
321 Radtke, H., Lipka, M., Bunke, D., Morys, C., Woelfel, J., Cahill, B., Böttcher, M.E., Forster, S., Leipe,
322 T., Rehder, G., Neumann, T., 2019. Ecological ReGional Ocean Model with vertically resolved
323 sediments (ERGOM SED 1.0): coupling benthic and pelagic biogeochemistry of the south-western
324 Baltic Sea. Geoscientific Model Development 12(1), 275-320. doi.org/10.5194/gmd-12-275-2019.
325 Soetaert, K., Herman, P.M.J., Middelburg, J.J., 1996. A model of early diagenetic processes from the
326 shelf to abyssal depths. Geochim. Cosmochim. Acta 60(6), 1019-1040. doi.org/10.1016/0016-
327 7037(96)00013-0.
328 Wang, J., Zhao, L., Fan, R., Wei, H., 2016. Scaling relationships for diffusive boundary layer thickness
329 and diffusive flux based on in situ measurements in coastal seas. Prog. Oceanogr. 144, 1-14.
330 doi.org/10.1016/j.pocean.2016.03.001.
331 Wang, X.H., 2002. Tide-Induced Sediment Resuspension and the Bottom Boundary Layer in an Idealized
332 Estuary with a Muddy Bed. Journal of Physical Oceanography 32(11), 3113-3131.
333 doi.org/10.1175/1520-0485(2002)032<3113:Tisrat>2.0.Co;2.
334 Yamaguchi, H., Hirade, N., Kayama, M., Ichimi, K., Tada, K., 2014. Total organic carbon and nitrogen
335 contents in surface sediments of Harima Nada, eastern Seto Inland Sea, Japan: a comparison under two
336 different trophic states. Journal of Oceanography 70(4), 355-366. doi.org/10.1007/s10872-014-0235-7.